Title: Rapid endothelialitis and vascular inflammation characterise SARS-CoV-2 infection in a human lung-on-chip model

[VIVEK V THACKER *[1], KUNAL SHARMA ^[1], NEERAJ DHAR ^[1], GIAN-FILIPPO MANCINI[2], JESSICA SORDET-DESSIMOZ[2], JOHN D MCKINNEY[1]]

[1]Global Health Institute, Ecole Polytechnique Federale de Lausanne, Switzerland

[2] Histology Core Facility, Ecole Polytechnique Federale de Lausanne, Switzerland

^ equal contribution

*Corresponding author: Vivek V Thacker, vivekvthacker@gmail.com

Abstract

Background: Severe manifestations of COVID-19 include hypercoagulopathies and systemic endothelialitis. The underlying dynamics of damage to the vasculature, and whether it is a direct consequence of endothelial infection or an indirect consequence of immune cell mediated cytokine storms is unknown. This is in part because *in vitro* infection models are typically monocultures of epithelial cells or fail to recapitulate vascular physiology.

Methods: We establish a vascularised lung-on-chip infection model consisting of a co-culture of primary human alveolar epithelial cells ('epithelial') and human lung microvascular endothelial cells ('endothelial'), with the optional addition of CD14+ macrophages to the epithelial side. A combination of qRT-PCR, RNAscope, immunofluorescence, and ELISA measurements are used to study the dynamics of viral replication and host responses to a low dose infection of SARS-CoV-2 delivered to the apical surface of the epithelial face maintained at an air-liquid interface.

Findings: SARS-CoV-2 inoculation does not lead to a productive amplification of infectious virions. However, both genomic and antisense viral RNA can be found in

1

endothelial cells within 1-day post infection (dpi) and persist upto 3 dpi. This generates an NF-KB inflammatory response typified by IL-6 secretion and a weak antiviral interferon response even in the absence of immune cells. Endothelial inflammation leads to a progressive loss of barrier integrity, a subset of cells also shows a transient hyperplasic phenotype. Administration of Tocilizumab slows the loss of barrier integrity but does not reduce the occurrence of the latter.

Interpretation: Endothelial infection can occur through basolateral transmission from infected epithelial cells at the air-liquid interface. SARS-CoV-2 mediated inflammation occurs despite the lack of rapid viral replication and the consequences are cell-type dependent. Infected endothelial cells might be a key source of circulating IL-6 in COVID-19 patients. Vascular damage occurs independently of immune-cell mediated cytokine storms, whose effect would only exacerbate the damage.

Introduction

Organ-on-chip technologies recreate key aspects of human physiology in a bottom-up and modular manner[1]. In the context of infectious diseases, this allows for studies of cell dynamics[2,3], infection tropism[4], and the role of physiological factors in disease pathogenesis in more native settings[5]. This is particularly relevant for the study of respiratory infectious diseases[6], where the vast surface area of the alveoli poses a challenge to direct experimental observation.

COVID-19, caused by the novel *betacoronavirus* SARS-CoV-2, first manifests as an infection of the upper airways. Severe cases are marked by progression into the lower airways and alveoli. Here, it manifests as an atypical form of acute respiratory distress syndrome (ARDS) characterized by good lung compliance measurements[7,8], and elevated levels of coagulation markers such as D-dimers[9], and pro-inflammatory markers in the blood[10]. Autopsy reports show numerous microvascular thrombi in the lungs of deceased patients together with evidence of the intracellular presence of the virus in vascular cells[11,12]. These suggest that the lung microvasculature plays a key role in COVID-19 pathogenesis[13], yet most in vitro studies have focused on monocultures of upper airway respiratory cells. In studies with alveolar epithelial cells, SARS-CoV-2 has been shown to replicate poorly both in the A549 lung adenocarcinoma cell line[14] and in primary alveolar epithelial cells *ex vivo*[15] and has been reported to be unable to infect primary microvascular endothelial cells[16], which are at odds with the reported medical literature. There is therefore an urgent need for a better understanding of the pathogenesis of SARS-CoV-2 in alveolar epithelial cells and in a more realistic model of the alveolar space that is vascularized. The lung-on-chip model is well-suited to this purpose because it includes a vascular compartment maintained under flow, and infection can occur at the air-liquid interface, two key

physiological features that are lacking in organoid models[17–19]. We therefore establish a human lung-on-chip model for SARS-CoV-2 infections, and probe the viral growth kinetics, cellular localization and responses to a low dose infection using qRT-PCR, ELISA, RNAscope, immunofluorescence and confocal imaging (Fig. 1J).

Results

SARS-CoV-2 infection alters relative expression of viral entry factors on-chip

We established a human lung-on-chip model for SARS-CoV-2 pathogenesis (Fig. 1A) using primary human alveolar epithelial cells ('epithelial') and lung microvascular endothelial cells ('endothelial'), which form confluent monolayers on the apical and vascular sides of the porous membrane in the chip (Fig. 1B, C). The modular nature of the technology allowed us to recreate otherwise identical chips either with (Fig. 1B) or without ('w/o') the addition of CD14+ macrophages to the epithelial layer on the apical side of the chip. We first characterized the epithelial and endothelial cells used, both in monoculture (Fig. S1A) and on-chip after 1 day at air-liquid interface (Fig. 1D) to understand how air-liquid interface and co-culture may alter the expression of SARS-CoV-2 entry factors. In epithelial cells, *ACE2* expression was low both in monoculture (Fig S1A) and on-chip (Fig 1D) consistent with transcriptomic[16,20] and proteomic analyses[21] of human tissue. Expression on-chip was five-fold lower than monoculture (Fig. S1B). *ACE2* expression was 60-fold lower in endothelial cells versus epithelial cells in monoculture (Fig. S1A), although expression increased 10-fold on-chip (Fig. S1B), likely due to the effects of shear stress and flow in the vascular channel[22]. Neuropilin-1, an integrin-binding protein[23] has recently been reported to be an alternative receptor for SARS-CoV-2 entry[24,25]. *NRP1* expression was between one and four orders of magnitude higher than *ACE2* expression both in monoculture and on-

4

chip (Fig. S1A, 1D), with a10-fold higher expression in endothelial cells compared to epithelial cells that was retained on-chip (Fig S1B). Expression of cell surface receptor proteins used for SARS-CoV-2 entry in both cell types differs significantly in co-culture at an air-liquid interface, and an alternative entry receptor such as *NRP1* are far more expressed than *ACE2*.

A low dose infection (100 plaque forming units, multiplicity of infection (MOI)=0.001) of the apical surface of the LoC reduced *NRP1* expression in both cell types at 1 dpi(Fig. 1E, F, S1C). Although a change in *ACE2* expression was not observed in epithelial cells at 1 dpi, expression in the epithelial layer declined over subsequent days as measured using RNAscope assays (Fig. 1 F, G, H, p=0.014). Interestingly, infection significantly increased expression of the TMPRSS2 protease[26] at 1 dpi in both cell types relative to both on-chip controls at air-liquid interface (Fig. 1 E, I) and monoculture (Fig. S1C), which may explain how infection spreads through the alveolar space despite overall low levels of *ACE2* expression.

Infection of the alveolar space is characterized by a lack of productive infection, cell-to-cell transmission, and slow intracellular replication

We first characterized the progression of infection by measuring the release of viral progeny and intracellular viral RNA loads. Infected LoCs were monitored daily for the release of infected viral progeny (1) *apically* – on the epithelial layer and (2) *basolaterally* - in the cell culture media flowed through the vascular channel ('apical wash' and 'vascular effluent' in Fig. 1A). A low number of viral genomes were released apically in the epithelial layer, and the number of genomes detected decreased over 1-3 dpi (Fig. 2A). Genome copy numbers were 100-fold lower than the starting inoculum

(100 PFU), suggesting that instances of productive infection were rare. No viral genomes were detected in the vascular effluent (Fig. 2B), and the lack of infectious particles in the effluent was confirmed for two LoCs with and w/o macrophages by plaque forming unit assays (data not shown). Nevertheless, total RNA extracted from the apical and vascular channels of an infected LoC without macrophages at 1 dpi revealed $>10^4$ genomes in both epithelial and endothelial cells (Fig. 2C) and genome copy numbers exceeded those for cellular housekeeping gene *RNAseP* (Fig. 2D). Similar numbers of viral genome copy numbers have been reported for infections of alveolar epithelial cell monoculture[15] and are modest in comparison to airway epithelial cells and Vero E6 cells[27]. Nevertheless, SARS-CoV-2 appears to disseminate rapidly from the epithelial to the endothelial layer. Basolateral transmission has not been reported to be the major mode of transmission for both SARS-CoV-2[28] and SARS-CoV-1[29] infections of monocultures of upper airway cells at the air-liquid interface. This suggests that basolateral transmission may either be a unique feature of alveolar epithelial cells or a consequence of cell-to-cell contact between epithelial and endothelial cells in our vascularised model.

SARS-CoV-2 infection of endothelial cells leads to increased permeability and loss of tight junctions

Autopsy reports show features of exudative alveolar damage[12]. The LoC model is compatible with microscopy-based assays which allowed us to assess changes in cellular physiology with high spatial resolution using confocal microscopy. We began by enumerating the number of nuclei per unit area of the membrane surface for LoCs at 1 and 3 dpi. In the epithelial layer, the density of nuclei declines progressively irrespective of the presence (p=0.010, p=9E-4) and absence (p=0.054, p=0.029) of

6

macrophages compared to uninfected controls(Fig. 3A). In contrast, the nuclear density

increases in the endothelial layer at 1 dpi before decreasing back to levels in the control

samples at 3 dpi (Fig. 3B). These results appeared counterintuitive and so we examined

if infection affected the morphology of the cells. Staining for F-actin localisation

revealed striking changes to the morphology of cells in the vascular channel. 3D views

of the endothelial layer from an uninfected control LoC also maintained at the air liquid

interface show a confluent layer of cells aligned with the long axis of the channel as

expected (Fig 3C, Fig. S2A). However, in infected LoCs there are clear signs of

vascular inflammation (Fig 3D-E). At 2 dpi, areas of cellular hyperplasia characterised

by an increased cell density and stronger nucleic acid staining (Fig 3D, yellow arrows)

coexist with areas with normal nucleic acid staining levels but reduced cell-to-cell

contact (Fig 3D, white arrows). By 3 dpi, a significant loss of tight junctions and cell

confluency is observed (Fig 3E, Fig S2B-D). Vascular cells form clusters, and a much

larger proportion of the surface area of the chip has low or no actin staining compared

to the uninfected control (Fig. S2E). In stark contrast, for the same chip, the epithelial

layer maintains a high degree of confluency (Fig, 3F, Fig. S2F).

Immunostaining for the viral S protein at 3 dpi (Fig 3G for endothelial and Fig 3H for

epithelial layers, additional examples in Fig. S2B-D, F) together with the zooms show

clear evidence of individual infected epithelial (Fig. 3I) and endothelial cells (Fig. 3J).

In some cases, S proteins appear to co-localize with the periphery of the nucleus (Fig.

3I, 3J, white arrows). The transfer of viral proteins from the apical to basolateral

channels can be better appreciated from a 3D view of the two channels together with

the connecting pores in the PDMS membrane; S protein can be clearly localised to the

interface of the two cell types in the pores of the membrane (yellow arrows, Fig, 3K).

Despite low levels of infection, epithelial and endothelial cells have very different

physiological responses, and vascular injury by 3 dpi was a consistent observation across all LoCs in this study.

In stark contrast, monoculture infections with viral innocula up to 100 fold greater than the apical inoculum used in the LoC experiments (Fig. 2A) showed few foci of viral S proteins. Endothelial cells retained their morphology and confluency (Fig. S3) up to 2 dpi, in agreement with recent reports of the inability of apical inoculations of SARS-CoV-2 to infect lung microvascular endothelial cells [16]. This confirms that the site of infection of endothelial cells (apical vs basolateral) is important – a physiological factor that can be recapitulated in the LoC but not in simpler models.

SARS-COV-2 persists in individual epithelial and endothelial cells in the alveolar space

We used RNAscope together with confocal microscopy to probe the spatial distribution and cell-to-cell variability of viral RNA and antisense RNA generated during viral replication *in situ* using probes for *S* RNA and *ORF1AB* antisense RNA respectively. Representative images for 232 x 232 μm^2 fields of view from the apical and vascular channels of chips at 1 and 3 dpi are shown in Fig 4A-H. At 1 dpi, a few examples of heavily infected cells are visible on the epithelial layer (Fig. S4A-C) and viral genomic RNA can be detected throughout the cytoplasm. These cells are likely to be the source of infectious virions released in the apical wash in Fig. 2A. However, in the vast majority of cells on the epithelial layer, the virus is detected only at low levels at 1 dpi (Fig. 4A), and infection does not appear to be limited by (Fig. 4C, white arrows) or even correlated to cellular *ACE2* expression at the time of fixation (Fig. 4D, yellow arrows). Both genomic and antisense RNA are detected in endothelial cells at 1 dpi

8

(Fig. 4B), indicating that intracellular viral replication can also occur in these cells. Heavily infected endothelial cells were not observed, in agreement with the lack of infectious virions in the vascular effluent (Fig. 2B). Areas of hyperplasia can be observed, and zooms (Fig 4E, F) show examples of viral infection of endothelial cells with and without the hyperplasic phenotypes. As with the epithelial layer, instances of localization of viral RNA with the nucleus is also observed (Fig. 4 F, white arrowheads). At 3 dpi, infection in both layers (Fig 4G, 4H) and the loss of endothelial layer integrity is evident (compare Fig, 4G vs Fig. 4H). We did not detect heavily infected epithelial cells at 3 dpi, in agreement with the diminishing viral titer (Fig. 2A).

We normalized the number of RNA dots detected either on a per-cell basis (Fig. 4I-K) or per-field-of-view basis (Fig. S5), to enable quantification of differences between the two layers while accounting for differences in cell numbers and cell death. The median values of intensities were similar across all conditions (Fig. S6). In the epithelial layer, in of viral infection and replication per cell were either similar (Fig. 4 J, L) or lower by 3 dpi (Fig. 4I, p=0.018; Fig. 4K, p=0.006). In contrast, viral RNA accumulates in individual endothelial cells (Fig. 4K, Fig. 4L, p=0.004). The presence of macrophages generally leads to lower levels of viral RNA replication (Fig. 4I, J) but does not prevent the accumulation of viral genomes intracellularly in endothelial cells (Fig. 4L). At 3 dpi, *ACE2* levels are higher on a per-cell basis in endothelial vs epithelial cells (Fig. 4M, p=0.028), due to a reduction in *ACE2* levels on the epithelial layer.

Normalization on per-field-of-view shows predominantly a *declining* trend for levels of replication (Fig. S5A, B) and intracellular viral RNA (Fig, S5C,D) in both cell types, as well as a decline in *ACE2* expression (Fig. S5E,F). These results highlight the cumulative effect of differential cell numbers and cell death in these two layers (Fig.

3A, B). Overall, virus levels are low and decline in both layers by 3 dpi, yet the virus persists and continues to replicate within individual infected cells, in agreement with reports of clinical infection.

Persistent NF-KB inflammatory response to SARS-CoV-2 infection in endothelial but not epithelial cells

Concurrently, we investigated host responses to the infection. No IL-6 was detected in the vascular effluent from uninfected controls, whereas IL-6 secretion was observed up to 3 dpi in LoCs both in the presence or absence of macrophages (Fig. 5A). Interestingly, IL-6 levels were not significantly different between these two categories of LoCs, which suggested a non-immune cell source for this cytokine (Fig. 5A). ELISA assays for IL-1B and IP10 did not detect these cytokines in the effluent (data not shown). Expression levels of pro-inflammatory genes (*TNFA*, *IL6*, *IL1B*) at 1 dpi was an order of magnitude higher than that of interferon genes in both cell types, and little to no interferon stimulatory gene expression was detected in both cell types (Fig. 5B), consistent with the lack of detection of IP10 via ELISA. Responses were also cell-type specific; endothelial cells from infected LoCs showed upregulation of inflammatory genes and interferon genes but a downregulation of *IP10* and *ISG15* expression (Fig. 5C) whereas expression of inflammatory cytokines in epithelial cells was lower than in controls (Fig. S7). The lack of IL-1B secretion despite high expression (Fig. 5B), suggests that it is not exported[30].

We used RNAscope to probe the spatial distribution of *IL6* expression in LoCs reconstituted with macrophages to verify the sources of expression. Consistent with the qRT-PCR data, *IL6* expression in the control LoC is higher in the epithelial layer (Fig. S8A) than the endothelial layer (Fig. S8B). At 1 dpi, individual cells with high levels

10

of *IL6* expression were observed in both epithelial and endothelial layers (Fig. 5D, E). Subsequent immunostaining with an anti-CD45 antibody confirmed that the *IL6* expression in the epithelial layer of the chip did not co-localise with macrophages either in controls (Fig. S8A, B) or upon infection (Fig. S8 C-E).

By 3 dpi *IL6* expression in the epithelial layer had returned to the control levels (Fig. 5F, L, S9A) whereas expression increased dramatically and was more widespread in the endothelial layer (Fig. 5G, L S9A, S9B). Expression did not appear to correlate with level of infection – zooms of cells with comparable levels of infection in Fig. 5G with low (Fig. 5H), medium (Fig. 5I) and high (Fig. 5 J, K) *IL6* expression are shown. Expression at 3 dpi was higher than that at 1 dpi, the epithelial layer at 3 dpi, and the uninfected controls, both on a per-cell and per-field-of-view basis (Fig. 5L, Fig. S9A p=0.004, p=0.014, p=0.008 respectively). Unlike viral RNA levels (Fig. S5B, D) *IL6* expression in the endothelial layer *does not diminish* over 1-3 dpi and would therefore appear to be the major contributor to IL-6 secretion in the vascular effluent.

Given the pleiotropic nature of IL-6[31], we also examined expression of the IL6R receptor and the metallopeptidase ADAM17 which sheds the TNF-alpha receptor and the IL-6R receptor[32] in the endothelial layer at 1 dpi. *IL6R* expression was low (Fig. 5M) and was not altered by infection, whereas *ADAM17* expression was high (Fig. 5M) and was increased 40-fold over uninfected controls (Fig. 5N). ADAM17 has been shown to enhance vascular permeability[33], and so we reasoned that targeting *trans* IL-6 signalling using the anti-IL-6R monoclonal antibody Tocilizumab[34], that is also undergoing clinical trials as a repurposed therapeutic for COVID-19, might ameliorate the vascular inflammation observed. Tocilizumab administration at 56 μg/mL via continuous perfusion *per se* did not abrogate IL-6 secretion (Fig. 5A). An investigation of cell morphologies in the endothelial layer also showed that the perfusion *did not*

prevent the occurrence of hyperplasia (Fig. 6A, zooms in Fig. 6C, control in Fig. 6D, zoom in Fig. 6F) but the remaining cells of the endothelial layer retained tight-junction formation to a greater extent (Fig. 6A, zooms in Fig. 6B, control in Fig. 6D, zoom in Fig. 6E). To quantify this, we compared regions of interest (ROIs) that excluded areas of cellular hyperplasia across at least six fields of view from the endothelial layer of LoCs with and without Tocilizumab perfusion, and identified areas with low or no F-actin staining as those with reduced confluence, as in Fig. S2E. A plot of the proportion of pixels with intensities below a defined cut-off threshold (Fig. 6G) showed that the untreated LoC had a significantly higher proportion of pixels with intensities lower than 5% (p=0.032) of the maximum intensity (p=0.022 for 3% and p=0.038 for 2%). Inhibition of IL-6 signalling through Tocilizumab is able to ameliorate some but not all of the vascular damage observed.

Discussion

SARS-CoV-2 infection of the alveolar space results in strikingly different outcomes from upper airway respiratory models. Because most virology assays measure viral titre, studies with alveolar epithelial cell lines have increased *ACE2* expression through transfection or infected at high MOI[14]. In contrast, we use an infectious dose more relevant to either direct aerosol inspiration or the transfer of virions from the upper respiratory tract. On-chip, this leads to slow viral replication and cell-to-cell spread of virus without significant release of infectious virions. This might be due to the significant increase in *TMPRSS2* expression, or the use of alternate receptors for viral entry such as NRP1. It has been speculated that high levels of *ACE2* expression may be necessary for export of mature virions [35], which would be consistent with the few foci of heavily infected cells and low numbers of viral titre detected on chip, yet why alveolar cells show persistent but not productive infection is still unclear.

Physiological factors play a prominent role in SARS-CoV-2 pathogenesis. Although SARS-CoV-2 has been shown to infect vascularised organoids at high MOI[36], we do not observe signs of infection in lung microvascular endothelial cells when directly exposed to the virus on their apical surface. Basolateral transmission has also not been reported to occur to a large extent in air-liquid interface cultures of airway epithelial cells. However, in co-culture, basolateral transmission from epithelial cells efficiently infects lung microvascular cells. This might occur through direct cell-to-cell contact, which occurs *in vivo* at the alveolar-capillary interface and in the pores of the membrane on-chip and represent an ACE2-independent mechanism of uptake. The consequences of this may extend downstream to the slow intracellular replication and enhanced inflammation observed.

Low levels of intracellular viral RNA generates an NF-KB mediated pro-inflammatory response, with suppression of antiviral interferon responses, consistent with reports of the effect of a number of viral proteins[37,38]. Yet, a striking observation is the differing response of epithelial and endothelial cells – inflammation in epithelial cells is transient, whereas it is persistent in endothelial cells. Within these cell types, there are significant cell-to-cell differences in expression of inflammatory markers, clearly identifiable with good spatial resolution through the use of RNAscope and confocal imaging in the LoC model. These differences could be due to differences in the mode of uptake – NRP1 is also a receptor for VEGF signalling[39], or differences in the intracellular localization of viral RNA and RNA replication, or differences in the levels of translation of viral proteins. We observe instances of co-localisation of viral RNA and S protein with the nucleus, which is consistent with bioinformatic predictions using algorithms for RNA localisation[40], but has not been reported in studies using cell lines with productive

infections. These atypical sub-cellular localisations may be characteristic of persistent infection and merit further investigation.

Crucially, these differences also manifest on the level of cellular morphology: low-levels of infection can nevertheless profoundly alter the morphology of endothelial cells and lead to a loss of confluence, which would activate the intrinsic coagulation pathway *in vivo*. This suggests that the hypercoagulatory phenotype in COVID-19 patients is partly due to the direct infection of endothelial cells in the lung microvasculature, which would be aggravated by a subsequent influx of inflammatory immune cells *in viv*o and generate the exudative alveolar damage observed.

Lastly, our microscopy-based approach reveals that Tocilizumab perfusion reduces the occurrence of vascular permeability but does not prevent a subset of endothelial cells from over-proliferating and acquiring an inflammatory phenotype. This offers insights into reasons why, although the drug has been shown to reduce recovery times, there is insufficient evidence of the efficacy of Tocilizumab in reducing mortality, including in recent reports from the COVACTA trial. This highlights the ability of the model to make clinically relevant predictions.

In sum, SARS-CoV-2 infection of a model of the alveolar space shows a set of unique characteristics underlined by persistent infection, low viral replication, inflammatory response, and damage to endothelial layer integrity that are in good agreement with reports of clinical disease. The superior physiological mimicry LoC model (air-liquid interface, co-culture, perfusion through a vascular channel) reveals a number of insights into the dynamics and mechanisms that underlie these observations that are difficult to obtain in other experimental models and that we hope will improve our understanding of the pathogenesis of this multi-organ disease.

Acknowledgements

Methods

Cell culture

Primary human alveolar epithelial cells (epithelial cells) and human lung microvascular endothelial cells (endothelial cells) were obtained from a commercial supplier (Cell Biologics, USA). Each vial of epithelial cells consisted of a mix of Type I and Type II cells at passage 3, and expression of these markers was verified via qRT-PCR on-chip (Fig. 1D, E). Both cell types were cultured *in vitro* in complete medium comprising base medium and supplements (Cell Biologics, USA) in 5% CO_2 at 37°C. Passage of epithelial cells lowered *ACE2* expression (Fig. S1A), therefore all chips were reconstituted with epithelial cells seeded directly on the lung-on-chip (see below), without any additional *in vitro* culture. In contrast, we observed no significant changes in viral entry factor expression in endothelial cells upon passage, and so therefore these cells passaged between 3-5 times before seeding in the LoC devices.

PBMC isolation and macrophage differentiation

Peripheral blood mononuclear cells were obtained from buffy coat (Interregional Blood Transfusion SRC Ltd, Switzerland) obtained from anonymised donors. PBMCs were isolated using a Biocol Separation procedure as per the manufacturer's instructions. Isolated PBMCs were subsequently cryopreserved in a solution of 70% heat inactivated Fetal Bovine Serum (FBS, Gibco), 20% RPMI Medium (Gibco) and 10% dimethlysulfoxide (DMSO). One week prior to seeding the macrophages in the LoC devices, a cryopreserved aliquot was thawed and cultured in a T-75 flask (TPP, Switzerland) in RPMI supplemented with 10% FBS. CD14+ monocytes were isolated using positive selection (CD14 ultrapure isolation kit, Miltenyi Biosciences) and cultured in RPMI medium supplemented with 10%

15

FBS and differentiated for 7 days with 20 ng/ml recombinant human Macrophage-Colony Stimulating Factor protein (M-CSF) (Thermo Fisher Scientific), and 100U/L of penicillin-streptomycin solution (Thermo Fisher Scientific) to avoid bacterial contamination. The cells were cultured in plastic petri dishes without pre-sterilisation (Greiner Bio-One) so that differentiated macrophages could be more easily detached.

Quantitative Real-Time PCR (qRT-PCR) for cell characterization

Freshly isolated AECs (NS) were grown overnight in cell-culture microdishes (Ibidi) or T-25 cell culture flask (TPP, Switzerland). Passaged AECs (DS) were grown to confluency in a T-75 cell culture flask (TPP). Growth media was removed from the flask, and the cells were incubated with the appropriate volume of RNA lysis buffer (RNAeazy, Qiagen) and RNA isolated as per the manufacturer's instructions and resuspended in 25 µl of DEPC-treated water. Approximately 1 µg of RNA was then used to generate cDNA using the SuperScript®IV First-Strand Synthesis System with random hexamers (Invitrogen), which was stored at -20°C. Specific primers for used for the qRT-PCR are listed in Table S1. qRT-PCR reactions were prepared with SYBR®Green PCR Master Mix (Applied Biosystems) with 500 nM primers, and 1 µl cDNA. Reactions were run as absolute quantification on ABI PRISM®7900HT Sequence Detection System (Applied Biosystems). Amplicon specificity was confirmed by melting-curve analysis.

Quantitative Real-Time PCR (qRT-PCR) for quantification of viral genomes in the supernatant

150 µL of cell-free supernatant was processed using a kit to extract viral RNA as per the manufacturer's instructions (NucleoSpin Dx Virus, Machery Nagel). For the vascular effluent, this was taken from the approximately 1.5 mL of effluent generated daily by the flow through the vascular channel. In the case of the apical wash, the 30 µL collected from the apical channel was further diluted in cell culture media up to 150 µL and subsequently processed. Viral RNA was eluted in 50mL of DEPC-treated water. 5 mL of RNA was then used in a one-step qRT-PCR kit for SARS-CoV-2 detection (2019-nCoV TaqMan RT-PCR kit, Norgen Biosciences) using primer and probe mixes corresponding to the nucleocapsid

(N2) gene and the host RNAseP genes. Primer sequences are those listed by the US Centre for Disease Control (CDC).

Generation of SARS-CoV-2 stocks

VeroE6 cells and a clinical isolate of SARS-CoV-2 were a kind gift from the lab of Prof Carolyn Tapparel at the University of Geneva. SARS-CoV2/Switzerland/GE9586/2020 was isolated from a clinical specimen in the University Hospital in Geneva in Vero-E6. Cells were infected and supernatant was collected 3 days post infection, clarified, aliquoted and frozen at -80°C and subsequently titrated by plaque assay in Vero-E6. Virus used for all experiments in this manuscript was at passage 3 in Vero E6 cells.

Human lung-on-chip (LoC) model

LoC made of polydimethylsiloxane (PDMS) were obtained from Emulate (Boston, USA).   Extracellular matrix (ECM) coating was performed as per the manufacturer's instructions. Chips were activated using ER-1 solution (Emulate) dissolved in ER-2 solution at 0.5 mg/ml (Emulate) and exposed for 20 minutes under UV light. The chip was then rinsed with coating solution and exposed again to UV light for a further 20 minutes. Chips were then washed thoroughly with PBS before incubating with an ECM solution of 150 µg/mL bovine collagen type I (AteloCell, Japan) and 30 µg/mL fibronectin from human plasma (Sigma-Aldrich) in PBS buffered with 15 mM HEPES solution (Gibco) for 1-2 hours at 37°C. If not used directly, coated chips were stored at 4°C and pre-activated before use by incubation for 30 minutes with the same ECM solution at 37°C. Endothelial cells were cultured overnight at 37°C and 5% CO_2 in T-75 cell culture flasks, detached with 0.05% Trypsin, concentrated to 5-10 million cells/ml, and seeded on the bottom face of the PDMS membrane. The chip was then incubated for a short period at 37°C to allow the endothelial cells to spread and subsequently seeded with AECs. Freshly isolated AECs were seeded directly from cryopreserved vials received from the supplier, each vial of 0.5 million cells could be used to seed two chips. To increase reproducibility, vials were pooled and used to seed multiple chips. The chip was incubated overnight with complete epithelial and endothelial media in the epithelial and endothelial channels, respectively, under static

17

conditions. The next day, the chip was washed and a reduced medium for the air-liquid interface (ALI) was flowed through the vascular channel using syringe pumps (Aladdin-220, Word Precision Instruments) at 60 μl/hour as described [41]. The composition of the ALI media used was as described in [41] but with an FBS concentration of 5%. The epithelial face was incubated with epithelial base medium with 1 μM dexamethasone (Sigma Aldrich) without FBS supplementation to promote tight junction formation and surfactant expression as reported in previous lung-on-chip studies[41,42]. Flow was maintained over 2-3 days with daily replacement of the medium on the epithelial face (with dexamethasone supplementation). At the end of this period, in LoCs reconstituted with macrophages, CD14+ macrophages differentiated for 7 days in M-CSF (described above) were detached from the petri dish using 2 mM ethylenediaminetetraacetic acid (EDTA, Sigma Aldrich) in PBS at 4°C as well as mechanical scraping, centrifuged at 300 g for 5 minutes, and resuspended in a small volume of epithelial cell media without dexamethasone. This solution containing macrophages was introduced onto the epithelial face and incubated for 30 minutes at 37°C and 5% CO_2 to allow macrophages to attach to the epithelial cells. Medium on the epithelial face was then removed and the chip was maintained overnight at an air-liquid interface (ALI). Chips were controlled to ensure that they successfully maintained the ALI overnight and were then transferred to the biosafety level 3 (BSL-3) facility for SARS-COV-2 infection. No antibiotics were used in any of the cell culture media for setting up the LoC model.

Tocilizumab perfusion in the LoC model

Tocilizumab/Rho-Actemra (Roche, 20 mg/mL in saline) for intravenous administration were a kind gift from Prof Thomas Hugle at the University Hospital in Lausanne, Switzerland (CHUV). We simulated a single dose of 8 mg/kg given to a person of bodyweight 70 kg and a blood volume of 5 liters to obtain a concentration of 56 μg/mL in the cell culture media. Tocilizumab perfusion was started immediately after infection and was flowed through the vascular channel of infected chips for a period of 2 days post infection.

Characterization of infection in LoCs

18

Uninfected LoCs were maintained at an ALI for either 1 day (for total RNA extraction (two LoCs without macrophages) or for upto 3 days for RNAscope characterization (one LoC each were reconstituted with and without macrophages) after addition of macrophages, during which time ALI medium was flowed through the endothelial channel at 60 µl/hour. In the case of the former, total RNA from the epithelial and endothelial layers was extracted separately by passing 350 µL of the lysis buffer reconstituted as per the manufacturer's instructions (RNeasy Plus Mini Kit, Qiagen) through easy layer. Complete detachment of the cells in each layer was verified via optical microscopy. RNA was eluted in 25 µL of DEPC-treated nuclease free water and used for subsequent qRT-PCR reactions.

In the case of LoCs processed for RNAscope, the chip was fixed for 1 hour using a fresh solution of 4% paraformaldehyde in phosphate buffered saline (PBS), and subsequently dehdryated in a sequence of washes with 50% EtOH, 70% EtOH, and 100 % EtOH. The chips were then stored in 100% EtOH at -20°C until processed for RNAscope at the Histology Cor Facility at EPFL.

Immunofluorescence characterization

Subsequently, macrophages in the control LoC were identified via immunofluorescence labelling. Briefly, the chips were incubated with a blocking solution of 2% Bovine Serum Albumin (BSA) in PBS ('blocking buffer'), followed by overnight incubation with the primary antibody: mouse anti-human CD45 (abcam NUMBER), or mouse anti-SARS-CoV-2 spike protein (Genetex, NUMBER) at a concentration of 1:100 in the blocking buffer at 4°C. The following day the chip was washed extensively with fresh blocking buffer before inoculation with the secondary antibody at a concentration of 1:300 for 1 hour at room temperature. The secondary antibodies used were: Donkey anti-mouse Alexa Fluor 488 (A21206, Thermo Fisher), or Donkey anti-mouse Alexa Fluor 568 (A10037, Thermo Fisher), or Donkey anti-mouse Alexa Fluor 647(A31573, Thermo Fisher), and were chosen to complement the fluorophores already assigned to RNAscope labelling. F-actin on both the epithelial and endothelial face was stained using Sir-Actin dye in the far-red (Spherochrome) at 1 µM for 30 minutes concurrently with

Hoechst staining, as described above. Confocal images were obtained on a Leica SP8 microscope in the inverted optical configuration at the EPFL BIOP core facility.

Infection of the LoC with SARS-CoV-2

LoCs for infection were assembled into a sealed Tupperware box modified to contain inlets and outlets for the flow of medium through the vascular channel was maintained throughout the course of the experiment by use of a syringe pump. On the day of the experiment, an aliquot of virus-containing supernatant was thawed from the stock at -80 ℃, and diluted approximately 35-fold in epithelial cell media without FBS to generate the inoculum that corresponded to an infectious dose of 100 plaque forming units (PFU) in a volume of 30 μL. 30 μL of this solution was then added to the apical channel of each LoC, and the LoC was incubated for an hour at 37°C and 5% CO_2 to enable infection. Thereafter, the medium in the apical channel was removed. The LoC was returned to air-liquid interface and the inlets of the infected chip were sealed with solid pins as a safety precaution. The media flowing through the vascular channel of each LoC was collected in a separate, sealed 15 mL Falcon tube, and each tube was emptied daily and the effluent stored at -80°C for further processing. At this time, the metal pins sealing the apical channel of each chip were removed, and 30 μL of epithelial cell media without FBS was briefly added to the channel before being withdrawn and collected as the 'apical wash'. The metal pins were reinserted and the LoCs returned to the cell culture incubator. Both the vascular effluent and the apical wash from each chip were collected for each day post infection.

Infection was terminated at specified time points either by treatment with the lysis buffer for RNA extraction (one LoC reconstituted without macrophages) or by fixing with freshly prepared 4% paraformaldehyde for a period of 1 hour (all other infected LoCs) for RNAscope assay preparation. The chips were then dehydrated as described above and immersed in 100 % EtOH before removal from the BSL-3 facility.

RNAscope Assay

RNAscope Multiplex Fluorescent V2 assay (Bio-techne, Cat. No. 323110) was performed according to manufacturer's protocol directly on chips. They were

hybridized with the control Hs 3plex positive control (Bio-techne, Cat. No. 320861) or a combination of the following probes V-nCoV2019-orf1ab-sense (Bio-techne, Cat. 859151), Hs-ACE2-C2 (Bio-techne, Cat. 848151-C2), V-nCoV2019-S-C3 (Bio-techne, Cat. 848561-C3), HS-Il1b-C1 (Bio-techne, Cat. 310361), and Hs-Il6-C2 (Bio-techne, Cat. No. 310371-C2) simultaneously at 40°C for 2 hours. The different channels were revealed with TSA Opal570 (Akoya Biosciences, Cat. No. FP1488001KT), TSA Opal650 (Akoya Biosciences, Cat. No. FP1488001KT) and TSA Opal690 (Akoya Biosciences, Cat. No. FP1497001KT). Cells were counterstained with DAPI and mounted with Prolong Gold Antifade Mountant (Thermo Fisher, P36930).

ELISA assays

Frozen Vascular effluent from infected chips was thawed, incubated at 58°C for 30 minutes to ensure sterilization, and then removed from the BSL-3 for further processing. Levels of human IL-6 were determined by enzyme-linked immunosorbent assays (BD Biosciences) as per the manufacturers instructions.

Confocal imaging and Image Analysis

Infected and control LoCs were imaged using a Leica SP8 confocal microscope with a white light laser. For chips processed via RNAscope and labelled with Opal 650 and Opal 690, the excitation and emission windows were carefully chosen to minimise overlap of signal. LoCs were imaged with a 25x water immersion objective (NA=0.95, Leica), with standard settings across chips labelled the same way. Z stacks were subsequently deconvolved using the Huygens Deconvolution Software (Scientific Volume Imaging) and 3D views were rendered using the FIJI ClearVolume plugin[43]. Custom-written software in MATLAB was used to segment and identify the 3D volume, mean intensity, and number of RNA dots in each field of view using the nestedSortStruct algorithm for MATLAB written by the Hughey Lab (https://www.github.com/hugheylab/nestedSortStruct, GitHub). Statistical analysis was performed using Origin 9.2 (OriginLabs) and p-values were calculated using a Kruskal-Wallis one-way ANOVA test, with the null hypothesis that the medians of each population were equal.

References

1   Bhatia SN, Ingber DE. Microfluidic organs-on-chips. *Nat Biotechnol* 2014; **32**: 760–72.

2   Thacker V V, Dhar N, Sharma K, Barrile R, Karalis K, Mckinney JD. A lung-on-chip infection model reveals an essential role for alveolar epithelial cells in controlling bacterial growth during early tuberculosis. *bioRxiv* 2020; : 2020.02.03.931170v2.

3   Villenave R, Wales SQ, Hamkins-Indik T, *et al.* Human Gut-On-A-Chip Supports Polarized Infection of Coxsackie B1 Virus In Vitro. *PLoS One* 2017; **12**: e0169412.

4   Ortega-Prieto AM, Skelton JK, Wai SN, *et al.* 3D microfluidic liver cultures as a physiological preclinical tool for hepatitis B virus infection. *Nat Commun* 2018; **9**: 1–15.

5   Grassart A, Malardé V, Gobba S, *et al.* Bioengineered Human Organ-on-Chip Reveals Intestinal Microenvironment and Mechanical Forces Impacting Shigella Infection. *Cell Host Microbe* 2019; **26**: 435-444.e4.

6   Torrelles JB, Schlesinger LS. Integrating Lung Physiology, Immunology, and Tuberculosis. *Trends Microbiol* 2017; **25**: 688–97.

7   Gattinoni L, Coppola S, Cressoni M, Busana M, Rossi S, Chiumello D. COVID-19 does not lead to a "typical" acute respiratory distress syndrome. *Am. J. Respir. Crit. Care Med.* 2020; **201**: 1299–300.

8   Marini JJ, Gattinoni L. Management of COVID-19 Respiratory Distress. *JAMA - J. Am. Med. Assoc.* 2020; **323**: 2329–30.

9   Yao Y, Cao J, Wang Q, *et al.* D-dimer as a biomarker for disease severity and mortality in COVID-19 patients: A case control study. *J Intensive Care* 2020;

8: 49.

10   Messner CB, Demichev V, Wendisch D, *et al.* Ultra-High-Throughput Clinical Proteomics Reveals Classifiers of COVID-19 Infection. *Cell Syst* 2020; **11**: 11-24.e4.

11   Ackermann M, Verleden SE, Kuehnel M, *et al.* Pulmonary vascular endothelialitis, thrombosis, and angiogenesis in Covid-19. *N Engl J Med* 2020; **383**: 120–8.

12   Carsana L, Sonzogni A, Nasr A, *et al.* Pulmonary post-mortem findings in a series of COVID-19 cases from northern Italy: a two-centre descriptive study. *Lancet Infect Dis* 2020; 3099(20)30434-5.

13   Teuwen LA, Geldhof V, Pasut A, Carmeliet P. COVID-19: the vasculature unleashed. *Nat. Rev. Immunol.* 2020; **20**: 389–91.

14   Blanco-Melo D, Nilsson-Payant BE, Liu WC, *et al.* Imbalanced Host Response to SARS-CoV-2 Drives Development of COVID-19. *Cell* 2020; **181**: 1036-1045.e9.

15   Hui KPY, Cheung MC, Perera RAPM, *et al.* Tropism, replication competence, and innate immune responses of the coronavirus SARS-CoV-2 in human respiratory tract and conjunctiva: an analysis in ex-vivo and in-vitro cultures. *Lancet Respir Med* 2020; **8**: 687–95.

16   Hou YJ, Okuda K, Edwards CE, *et al.* SARS-CoV-2 Reverse Genetics Reveals a Variable Infection Gradient in the Respiratory Tract. *Cell* 2020; **182**: 429-446.e14.

17   Huang J, Hume AJ, Abo KM, *et al.* SARS-CoV-2 Infection of Pluripotent Stem Cell-derived Human Lung Alveolar Type 2 Cells Elicits a Rapid Epithelial-Intrinsic Inflammatory Response. *bioRxiv* 2020; :

2020.06.30.175695.

18   Abo KM, Ma L, Matte T, *et al.* Human iPSC-derived alveolar and airway epithelial cells can be cultured at air-liquid interface and express SARS-CoV-2 host factors. *bioRxiv* 2020; : 2020.06.03.132639.

19   Youk J, Kim T, Evans K V, *et al.* Robust three-dimensional expansion of human adult alveolar stem cells and SARS-CoV-2 infection. *bioRxiv* 2020; **2**: 2020.07.10.194498.

20   Qi F, Qian S, Zhang S, Zhang Z. Single cell RNA sequencing of 13 human tissues identify cell types and receptors of human coronaviruses. *Biochem Biophys Res Commun* 2020; **526**: 135–40.

21   Hikmet F, Méar L, Edvinsson Å, Micke P, Uhlén M, Lindskog C. The protein expression profile of ACE2 in human tissues. *Mol Syst Biol* 2020; **16**. DOI:10.15252/msb.20209610.

22   Song J, Hu B, Qu H, *et al.* Upregulation of angiotensin converting enzyme 2 by shear stress reduced inflammation and proliferation in vascular endothelial cells. *Biochem Biophys Res Commun* 2020; **525**: 812–8.

23   Valdembri D, Caswell PT, Anderson KI, *et al.* Neuropilin-1/GIPC1 Signaling Regulates α5β1 Integrin Traffic and Function in Endothelial Cells. *PLoS Biol* 2009; **7**: e1000025.

24   Daly JL, Simonetti B, Antón-Plágaro C, *et al.* Neuropilin-1 is a host factor for SARS-CoV-2 infection. *bioRxiv* 2020; : 2020.06.05.134114.

25   Cantuti-Castelvetri L, Ohja R, Pedro L, *et al.* Neuropilin-1 facilitates SARS-CoV-2 cell entry and provides a possible pathway into the central nervous system. *bioRxiv* 2020; : 2020.06.07.137802.

26   Hoffmann M, Kleine-Weber H, Schroeder S, *et al.* SARS-CoV-2 Cell Entry

Depends on ACE2 and TMPRSS2 and Is Blocked by a Clinically Proven Protease Inhibitor. *Cell* 2020; **181**: 271-280.e8.

27 Chu H, Chan JF-W, Yuen TT-T, *et al.* Comparative tropism, replication kinetics, and cell damage profiling of SARS-CoV-2 and SARS-CoV with implications for clinical manifestations, transmissibility, and laboratory studies of COVID-19: an observational study. *The Lancet Microbe* 2020; **1**: e14–23.

28 V'kovski P, Gultom M, Steiner S, *et al.* Disparate temperature-dependent virus – host dynamics for SARS-CoV-2 and SARS-CoV in the human respiratory epithelium. bioRxiv. 2020; : 2020.04.27.062315.

29 Tseng C-TK, Tseng J, Perrone L, Worthy M, Popov V, Peters CJ. Apical Entry and Release of Severe Acute Respiratory Syndrome-Associated Coronavirus in Polarized Calu-3 Lung Epithelial Cells. *J Virol* 2005; **79**: 9470–9.

30 Lopez-Castejon G, Brough D. Understanding the mechanism of IL-1β secretion. Cytokine Growth Factor Rev. 2011; **22**: 189–95.

31 Tanaka T, Narazaki M, Kishimoto T. Il-6 in inflammation, Immunity, And disease. *Cold Spring Harb Perspect Biol* 2014; **6**: 16295–6.

32 Zunke F, Rose-John S. The shedding protease ADAM17: Physiology and pathophysiology. Biochim. Biophys. Acta - Mol. Cell Res. 2017; **1864**: 2059–70.

33 Dreymueller D, Martin C, Kogel T, *et al.* Lung endothelial ADAM17 regulates the acute inflammatory response to lipopolysaccharide. *EMBO Mol Med* 2012; **4**: 412–23.

34 Tanaka T, Narazaki M, Ogata A, Kishimoto T. A new era for the treatment of inflammatory autoimmune diseases by interleukin-6 blockade strategy. Semin. Immunol. 2014; **26**: 88–96.

35   Klein S, Cortese M, Winter SL, *et al.* SARS-CoV-2 structure and replication characterized by in situ cryo-electron tomography. *bioRxiv* 2020; : 2020.06.23.167064.

36   Monteil V, Kwon H, Prado P, *et al.* Inhibition of SARS-CoV-2 Infections in Engineered Human Tissues Using Clinical-Grade Soluble Human ACE2 In Brief Clinical-grade recombinant human ACE2 can reduce SARS-CoV-2 infection in cells and in multiple human organoid models. Inhibition of SARS-CoV-2 Infections in Engineered Human Tissues Using Clinical-Grade Soluble Human ACE2. *Cell* 2020; **181**: 905-913.e7.

37   Hadjadj J, Yatim N, Barnabei L, *et al.* Impaired type I interferon activity and inflammatory responses in severe COVID-19 patients. *Science (80-)* 2020; : eabc6027.

38   Thoms M, Buschauer R, Ameismeier M, *et al.* Structural basis for translational shutdown and immune evasion by the Nsp1 protein of SARS-CoV-2. *Science* 2020; published online July 17. DOI:10.1126/science.abc8665.

39   Guo HF, Vander Kooi CW. Neuropilin functions as an essential cell surface receptor. J. Biol. Chem. 2015; **290**: 29120–6.

40   Wu K, Zou J, Chang HY. RNA-GPS Predicts SARS-CoV-2 RNA Localization to Host Mitochondria and Nucleolus. *bioRxiv Prepr Serv Biol* 2020; : 2020.04.28.065201.

41   Hassell BA, Goyal G, Lee E, *et al.* Human Organ Chip Models Recapitulate Orthotopic Lung Cancer Growth, Therapeutic Responses, and Tumor Dormancy In Vitro. *Cell Rep* 2017; **21**: 508–16.

42   Huh D, Matthews BD, Mammoto A, Montoya-Zavala M, Hsin HY, Ingber DE. Reconstituting organ-level lung functions on a chip. *Science* 2010; **328**: 1662–

8.

43   Royer LA, Weigert M, Günther U, *et al.* ClearVolume: Open-source live 3D

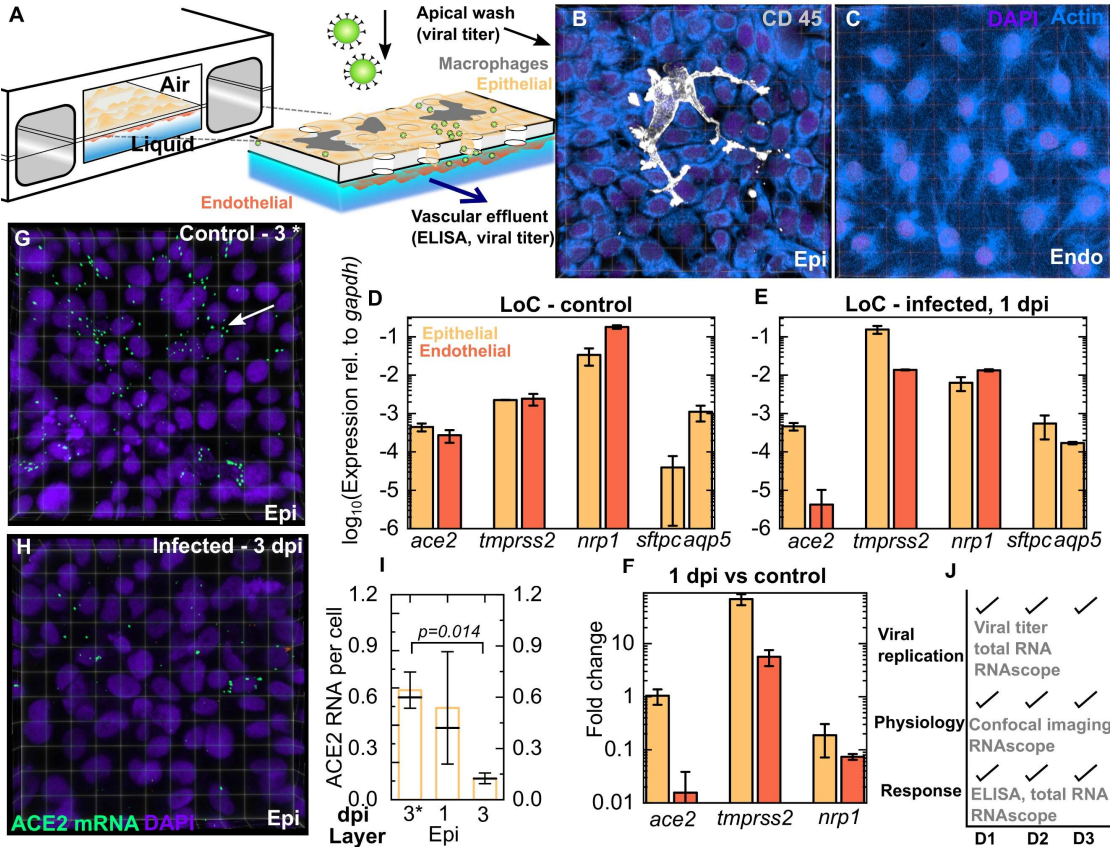visualization for light-sheet microscopy. Nat. Methods. 2015; **12**: 480–1.

Tables

Figures

Fig. 1. SARS-CoV-2 infection in a human lung-on-chip model. (**A**) Schematic of the LoC model for SARS-CoV-2. Confluent layers of epithelial and endothelial cells populate the top (**B**) and bottom faces (**C**) of the porous membrane. Where indicated, CD14+ macrophages (**B**) are also added to the epithelial layer. qRT-PCR characterization of the epithelial and endothelial layers on-chip for SARS-CoV-2 entry markers (*ACE2, TMPRSS2, NRP1*) as well as alveolar epithelial cell markers (*SFTPC, AQP5)* for cells extracted from the epithelial and endothelial layer from two uninfected LoC (**D**) and an infected LoC at 1 day-post infection (**E**), in both cases normalized to *GAPDH* levels. (**F**) A plot of the fold change in expression for viral entry factors at 1 day-post infection in the LoC model vs control. The bars in (**D-F**) represent the mean value, and the error bars represent the standard deviation. *ACE2* levels are also

characterize using RNAscope, a representative 3D view of a 232 x 232 μm^2 field of view of the epithelial face of an uninfected control at 3 days at air-liquid interface (3*) (**F**) and infected LoC at 3 dpi (**G**) are shown. The nucleus is labelled with DAPI, *ACE2* mRNA is labelled in green. (**H**) *ACE2* expression decreases between 1and 3 dpi in the LoC model, quantified on a per-cell basis for 4-5 fields of view in control and infected chips. The bars represent the mean value, the solid line represents the median value and the error bars represent the standard deviation. (**J**) An overview of the techniques used to characterize viral replication, physiological changes, and the cellular responses in the LoC over 3 days post infection. P-values are calculated using a Kruskal-Wallis one-way ANOVA test.
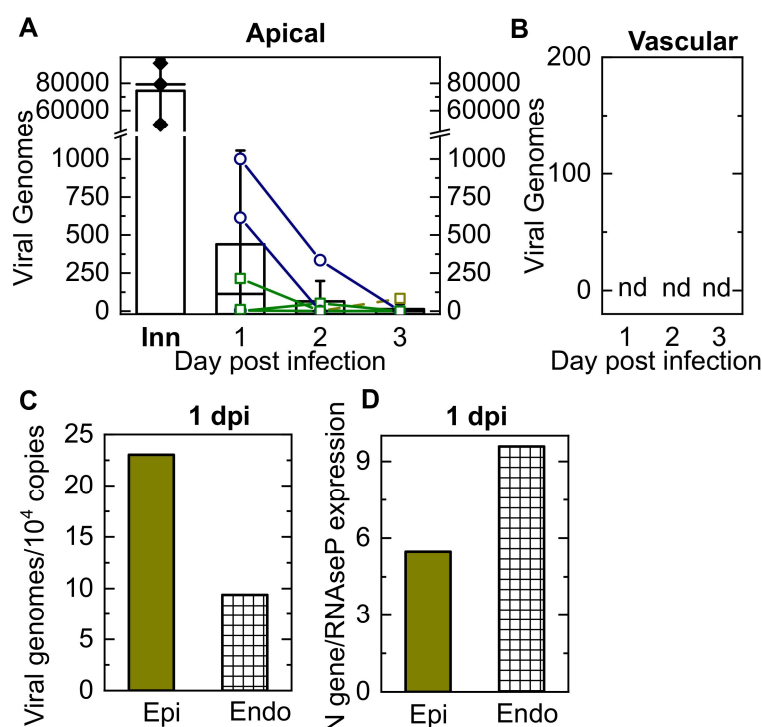
Fig. 2. Viral replication but lack of release of infectious virions characterizes SARS-CoV-2 infection in the LoC model. The kinetics of release of SARS-CoV-2 progeny was assessed from samples obtained from the apical face of the chip (**A**), and the vascular effluent (**B**) collected at each day-post infection. For each sample, viral RNA was extracted, and the number of genomes quantified using qRT-PCR for the N gene. The starting inoculum introduced to the apical side (labelled 'Inn') corresponded to 100 plaque forming units (PFU). Lines join datapoints from the same LoC, reconstituted with (green squares) and without (dark blue circles) macrophages. The height of the bars represents the mean, the solid black line represents the median, and error bars represent the standard deviation. Viral genome detection from the apical wash showed a declining trend over 3 days of infection. Viral genomes are not detected ('nd') in the vascular effluent (**B**) for all the chips shown in (**A**). A higher amount viral RNA is detected in the total RNA extracted from obtained from the apical and vascular channels respectively of an infected LoC without macrophages at 1 dpi (**C**). (**D**) Intracellular viral RNA levels at this timepoint relative to levels of the eukaryotic
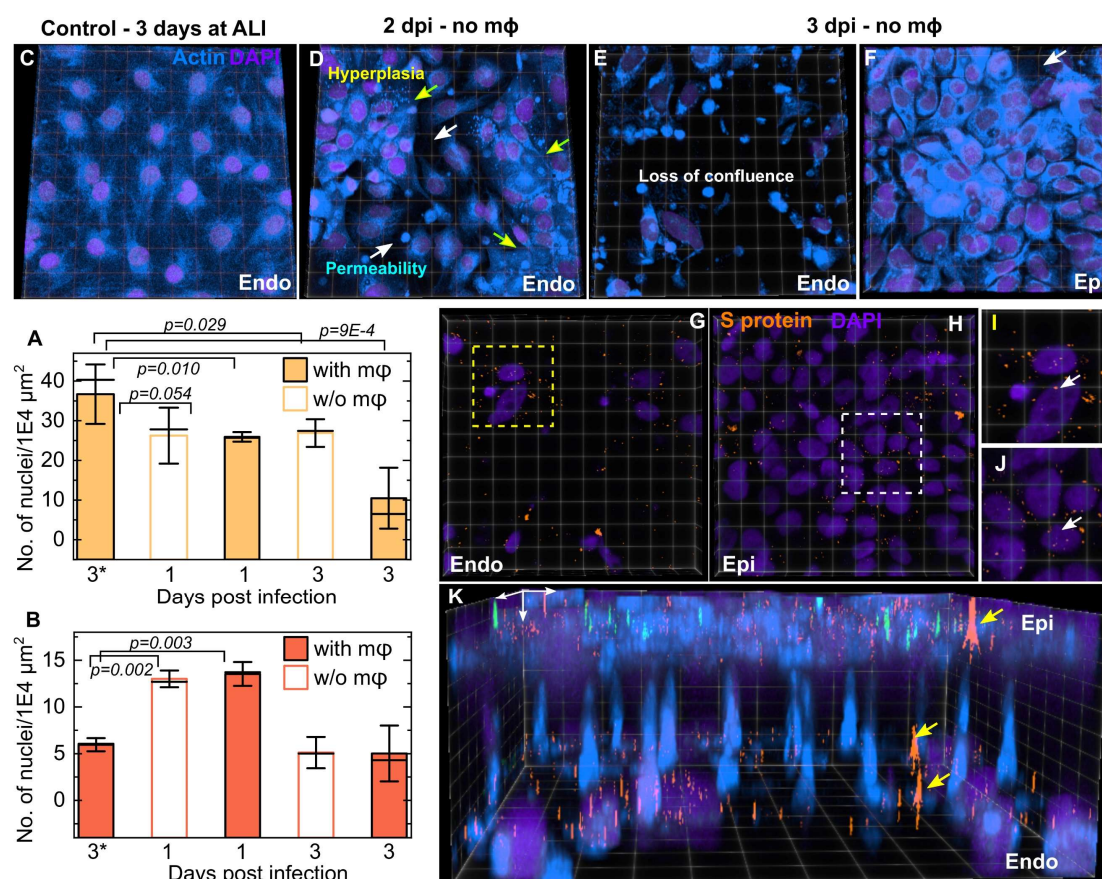
30

housekeeping gene *RNaseP*.

Fig. 3. SARS-CoV-2 infection disrupts endothelial barrier function. Plots of density of nuclei (number of nuclei per 1E4 μm^2) on the epithelial (**A**) and endothelial (**B**) faces of infected LoCs both with and without macrophages for characterization of the cellular layer integrity. The bars represent the mean value, the solid line represents the median and the error bars represent the standard deviation from at least 4 fields of view each from at least two independent LoCs for each timepoint. (**C-F**) 3D views of representative 232 x 232 μm^2 (**C, E**) and 155 x 155 μm^2 (**E, F**) fields of view from confocal imaging of an uninfected control (**C**), and infected chips without macrophages at days 2 (**D**) and 3 (**E, F**) post infection respectively. Actin and nuclear labelling are shown in azure and indigo, respectively. (**D**) At 2 dpi, adjacent areas of hyperplasic cell growth identified by a stronger nuclear stain and brighter actin staining (yellow arrows) and cells with increased permeability and loss of tight junctions (white arrows) are indicated. (**E, F**) At 3 dpi, a significant loss of barrier integrity is observed in the

endothelial layer, whereas the epithelial layer directly above this field of view is relatively intact. A small area of missing cells is shown in (**F**). The fields of view in (**E, F**) are shown also in (**G, H**) respectively, SARS-CoV-2 spike (S) proteins labelled via immunofluorescence are false-colored in amber. Zooms in (**I**) and (**J**) show clear evidence of intracellular spike protein within both endothelial and epithelial cells, respectively. A 3D view of the field of views in (**E, F**) and (**G, H**) respectively highlights the relative damage to the endothelial layer versus the epithelium, as well as the basolateral transmission of S protein via junctions in the pores of the membrane (identified with white arrows). P-values are calculated using a one-way Kruskal-Wallis ANOVA test.
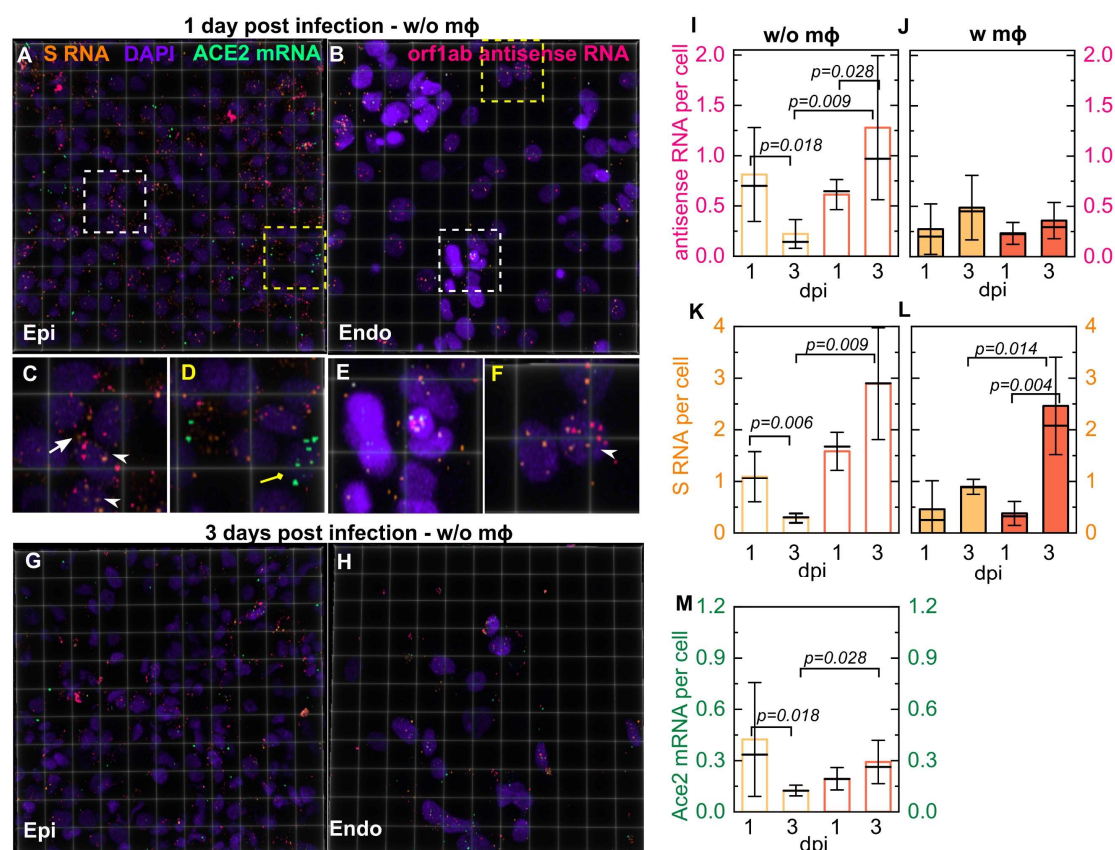
Fig. 4. RNAscope analysis reveals intracellular localization and slow accumulation of intracellular viral RNA in the LoC model. 3D views of 232 x 232 μm² fields of view of the epithelial (**A, G**) and endothelial layer (**B, H**) from infected LoCs reconstituted without macrophages at 1 (**A, B**) and 3 dpi (**G, H**). *Orf1ab* antisense RNA, *S* RNA, *ACE2* mRNA, and nuclear staining with DAPI are false-colored pink, amber, spring green, and electric indigo, respectively. (**C, D**) Zooms corresponding to the region in (**A**) highlighted with white and yellow boxes, respectively. (**C**) An example of infection and intracellular replication in a cell with no detectable *ACE2* expression (white arrow) as well as nuclear localization of viral RNA (white arrowhead). (**D**) An example of an uninfected cell with *ACE2* mRNA expression (yellow arrow). (**E, F**) Zooms corresponding to the regions in (**B**) representing increased nucleic acid staining (hyperplasic) and normal levels of nucleic acid staining highlighted with white and yellow boxes, respectively. (**E**) Examples of infection of hyperplasic endothelial cells

34

both with and without *ACE2* expression (**F**) Examples of endothelial cell infection with no *ACE2* expression, nuclear localization of viral RNA in an infected endothelial cell is indicated (white arrowheads). Quantification of viral antisense RNA (**I, J**) and viral genomic RNA (**K, L**) from pairs of otherwise identical LoCs reconstituted without (**I, K**) and with macrophages (**J, L**) analyzed at 1 and 3 dpi. Plots show the number of spots normalized by the total number of cells in 4-6 field of views detected using RNAscope and confocal imaging using identical imaging conditions for all chips. Bars represent the mean value, the solid line represents the median, and error bars represent the standard deviation. (**M**) Quantification of *ACE2* expression per cell in epithelial cells and endothelial cells in LoCs reconstituted without macrophages at 1 and 3 dpi respectively. P-values are calculated using a Kruskal-Wallis One-Way ANOVA Test.
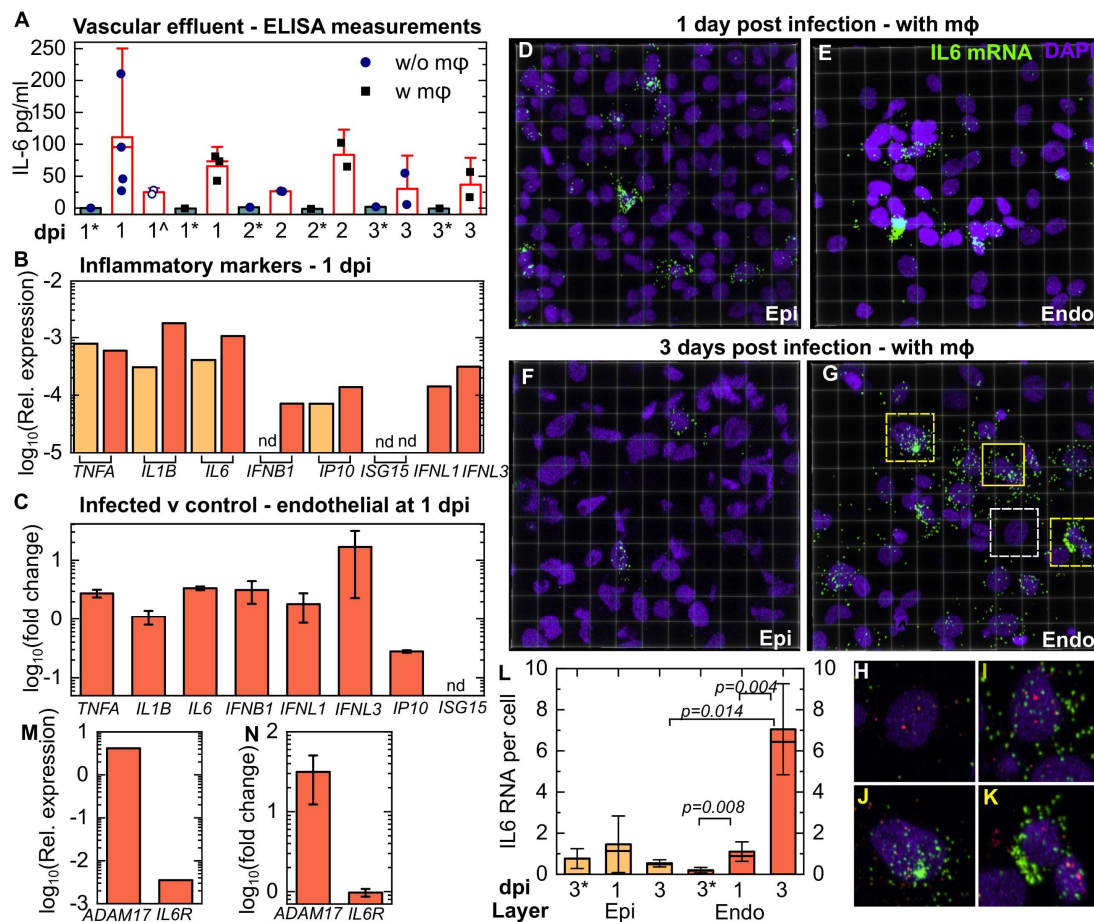
Fig. 5. SARS-CoV-2 infection generates a persistent pro-inflammatory response in endothelial cells. (A) Enzyme-linked immunosorbent assay (ELISA) measurements for IL-6 in the vascular effluent for at least two infected LoCs at each timepoint reconstituted with and without macrophages. Uninfected controls for each condition are indicated by * and grey bars, and LoCs with Tocilizumab administration are indicated by ^. The height of the bars represents the mean, the median is represented by a solid line, and the error bars represent the standard deviation. Each dot represents the mean of two technical replicates. **(B)** Relative expression of pro-inflammatory cytokines (*TNFA, IL1B, IL6*), interferon (*IFNB, IFNL1, IFNL3* (for the endothelial layer only)) and interferon stimulating genes (*IP10, ISG15*) in the epithelial and endothelial layer of an infected LoC reconstituted without macrophages. Expression is normalized to

36

GAPDH levels in each layer. Representative 232 x 232 μm^2 fields of view of the epithelial (**A**) and endothelial layer. (**C**) Fold-change in the markers in (**B**) relative to uninfected controls at the same timepoint. The bar represents the mean and the error bars the standard deviation. (**D-G**) 3D views of representative 232 x 232 μm^2 fields of view of the epithelial (**D, F**) and endothelial layer (**E, G**) from infected LoCs reconstituted with macrophages at 1 (**D, E**) and 3 dpi (**F, G**). *IL6* mRNA, and nuclear staining with DAPI are false-colored chartreuse and electric indigo, respectively. (**H-K**) Zooms corresponding to the regions in (**G**) highlighted with white (**H**) and yellow boxes with solid (**I**) and dashed lines (**J**, **K**) respectively. In these panels, *orf1abantisense* RNA (pink) and *S* RNA (amber) are also shown. The panels show examples of cells with similar levels of viral infection but with no (**H**), intermediate (**I**) and high levels (**J, K**) of *IL6* expression. (**L**) Quantification of *IL6* expression in epithelial and endothelial cells from a pair of otherwise identical LoCs analyzed at 1 and 3 dpi, respectively. Plots show the total number of spots normalized by the number of cells in 4-6 fields of view detected using RNAscope assay using identical imaging conditions for all chips. Bars represent the mean value, the solid line represents the median, and error bars represent the standard deviation. Data from uninfected controls for 3 days at air-liquid interface is indicated by *. (**M**) Expression relative to GAPDH and (**N**) fold-change in expression relative to uninfected controls for IL6R and ADAM17 expression in the endothelial layer. The bar represents the mean and the error bars the standard deviation. P-values are calculated using a Kruskal-Wallis One-Way ANOVA Test.
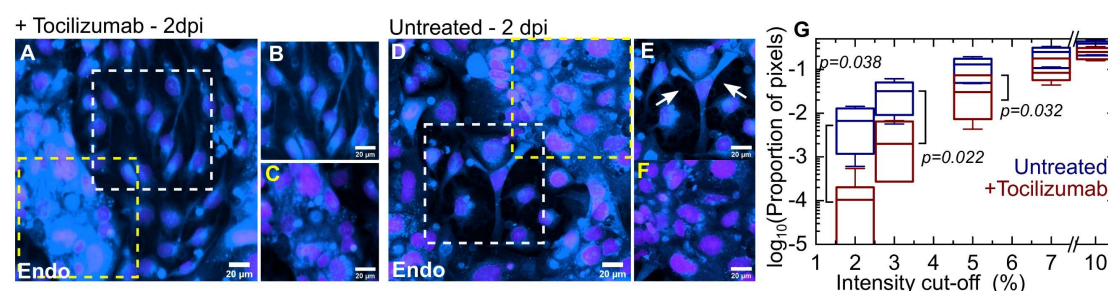
Fig. 6. Tocilizumab treatment preserves vascular cell junctions but does not prevent endothelial hyperplasia. Maximum intensity projections of representative 232 x 232 μm^2 fields of view of the endothelial layer from an infected LoC reconstituted without macrophages at 2 dpi with (**A**) and without Tocilizumab treatment (**B**). Actin and nuclear staining with DAPI are false-colored azure and electric indigo, respectively. (**B, C**) Zooms corresponding to the region in (**A**) highlighted with white and yellow boxes, respectively. (**B**) A region with normal vascular profile, endothelial cells are aligned along the axis of the LoC. (**C**) A region of hyperplasic cell growth. (**E, F**) Zooms corresponding to the regions in (**D**) representing regions highlighted with white and yellow boxes, respectively. (**E**) An example of reduced tight junctions between endothelial cells, bare patches are indicated with arrows. (**F**) A region of hyperplasic endothelial cell growth. (**G**) A plot of the proportion of pixels (shown on a logarithmic scale) with regions of low F-actin intensity identified via cut-off thresholds defined as a percentage of the maximum intensity in 6-7 regions of interest each for LoCs with and without Tocilizumab administration. ROIs were chosen from 232 x 232 μm^2 fields of view and were defined to exclude the occurrence of hyperplasic cells. A significantly larger fraction of the surface area of the ROIs for the untreated chips have low F-actin intensities. P-values are calculated using a Kruskal-Wallis One-Way ANOVA Test.